Forces and Flow Structures on a Simplified Car Model Exposed to an Unsteady Harmonic Crosswind

Valérie Ferrand

Forces and Flow Structures on a Simplified Car Model Exposed to an Unsteady Harmonic Crosswind

Valérie Ferrand
Université de Toulouse; Institut Supérieur de l'Aéronautique et de l'Espace (ISAE) ;
10 avenue Edouard Belin, 31400 Toulouse, France
valerie.ferrand@isae.fr

ABSTRACT

Ground vehicle travelling along a road is subject to unsteady crosswinds in a number of situations. In windy conditions, for example, the natural atmospheric wind can exhibit strong lateral gusts. Other situations such as tunnel exits or overtaking induce sudden changes in crosswinds, as well. The interaction of this unsteady oncoming flow with the vehicle and the resulting aerodynamic forces and moments affect the vehicle stability and comfort. The objectives of the current study are to improve the understanding of flow physics of such transient flow and ultimately to develop measurement techniques to quantify the vehicle's sensitivity to unsteady crosswind.

A squareback simplified car model is exposed to a forced oscillating yaw and results are compared to static measurements. Tests are conducted at Reynolds number $Re=3.7x10^5$ and reduced frequencies ranging from $0.265x10^{-2}$ to $5.3x10^{-2}$. Unsteady side force and yawing moment measurements are associated to Particle Image Velocimetry flow fields to interpret dynamic loads in link with flow topology evolution.

Phase average force and moment measurements are found to exhibit a phase shift between static and dynamic tests that increases with oscillating frequency. Velocity fields reveal that the

phase-shift seems to originate from the rear part of the car model. Moreover, lateral vortical structures appearing on lee side from $\beta=15°$ increase this phase-shift and consequently appear to be favourable to the lateral stability of the vehicle.

NOMENCLATURE

x_{CP} longitudinal position of the center of pressure (m)

f oscillation frequency

f* reduced frequency $f^* = \frac{fL_{ref}}{U_0}$

F_y side force (model coordinates system) (N)

F_{front} side force measured by the front load cell (N)

F_{rear} side force measured by the rear load cell (N)

Lref overall model length, reference length (m). Lref=0.28 m.

Ly model width (m)

M_Z yawing moment (model coordinates system) (N/m)

q_0 free stream dynamic pressure $q_0 = \frac{1}{2}\rho U_0^2$

Sref vehicle frontal area (m^2)

U_0 average free-stream velocity (m/s)

V velocity vector V=(U,V,W) :longitudinal, lateral and vortical component

(X,Y,Z) wind-tunnel coordinates system :longitudinal, lateral and vortical direction

(x,y,Z) model coordinates system

C_N yawing moment coefficient $C_N = \frac{2M_Z}{\rho U_0^2 S_{ref} L_{ref}}$

C_y overall side force coefficient $C_y = \frac{2F_y}{\rho U_0^2 S_{ref}}$

$C_{y\,front}$ front side force coefficient $C_{yfront} = \frac{2F_{yfront}}{\rho U_0^2 S_{ref}}$

$C_{y\,rear}$ rear side force coefficient $C_{yrear} = \frac{2F_{yrear}}{\rho U_0^2 S_{ref}}$

Re Reynolds number $Re = \frac{\rho L_{ref} U_0}{\mu}$

β yaw angle (°)

Ω_X steamwise component of the vorticity vector

ν air kinematic viscosity (m^2/s)

INTRODUCTION

A car travelling along a road is subject to unsteady crosswinds in a number of situations. In windy conditions, for example, the natural atmospheric wind can exhibit strong lateral gusts. Other situations such as tunnel exits or overtaking induce sudden changes in crosswinds, as well. The response of aerodynamic side force and yaw moment to a sudden change in lateral wind can present transient effects and lead to a potential source of hazard for drivers [1,2]. A common approach to predict these transient effects is based on the definition of the aerodynamic admittance function representing the ratio, in the spectral domain, between the side wind velocity turbulent components and the aerodynamic forces applying on a fixed body [3-7]. Despite being a reliable and well documented technique, this approach gives little information about the unsteady interaction between the flow and the vehicle.

A complete literature survey on experimental and numerical techniques available to simulate time-dependent crosswind can be found in [7-10]. The more realistic approach so simulate a wind gust on a ground vehicle consists in propelling a vehicle model on a rail trough the flow generated by a lateral wind tunnel [8,11-13]. This approach has been recently studied numerically using large eddy simulation [14, 15]. Whereas nearly all the authors show transient force overshoot compared to yawed vehicle steady force, little concordant results have been presented on the evolution of forces as a function of time, especially when discussing the entrance in the gust. Another approach to simulate gust propagation on a vehicle is the moving side jet facility studied both experimentally and numerically [10,16,17]. The model is fixed to the ground and the main wind tunnel is classically used to simulate the streamwise vehicle motion while a moving side jet produces the wind gust. This facility has supplied reliable measurements of unsteady aerodynamic efforts without any noise due to rail vibration from which suffers the previous approach. Moreover, the application of time resolved Particle Image Velocimetry offers very interesting new perspectives in the interpretation of transient aerodynamic forces apparition in link with unsteady flow development along the vehicle, as announced in the recent paper of Volpe et al [10]. Nevertheless, this method limits the analyse to one given step of yaw angle, while it appears useful to investigate and

compare cross wind effects in the whole yaw angle range potentially encountered on road, that is up to β=30°.

The experimental method applied in the current study consists of a model rotation about the vertical axis in a uniform upstream flow [18-20]. This approach does not directly simulate the side gust of wind, but allows for the analysis of flow and load responses when exposed to a dynamic yaw of various oscillating frequencies and mean yaw angles. A phase shift phenomena in the aerodynamic loads on bluff bodies for simulation of dynamic rather than quasi-static variation in yaw angle was observed in [18] but with no detailed explanation on responsible mechanisms. A coupling between vortex shedding and model stability has been suspected as a potential mechanism but with no formal proof [19]. In another experiment the wake of an oscillating vehicle was shown to exhibit significant sensitivity to yaw unsteadiness, at least within the explored range, β=-10° and β=+10° [20]. Drag calculated from wake data presented a phase shift between the dynamic and static approaches. However, side force or yawing moment, that are more relevant quantities to qualify crosswind sensitivity, were not available. Unsteady wall pressure distribution was recently investigated on realistic vehicle geometry under small amplitude yawing motion [21]. The observed difference between unsteady and steady side loads was attributed to the rear side of the vehicle. Recent numerical simulations of vehicle oscillation around the vertical axis offer new prospects in the interpretation of side loads unsteadiness in dynamic yaw ([22-24]). In other respects, unsteady bridge aerodynamics studies reported very similar phase shift between aerodynamic forces and instantaneous angle of attack [25,26]. Both measurements and numerical model show that non-linearities of the mean aerodynamics forces affect the unsteady force response to angle of attack fluctuations.

The current study proposes to enrich the experimental data base with unsteady side force and yawing moment measurements associated to Particle Image Velocimetry flow fields. The experimental facility presented in [20] is used for two yaw ranges. For the “low” yaw range $-10° \leq \beta \leq 10°$ the flow does not present any lateral separation whereas for the “high” yaw range $10° \leq \beta \leq 30°$, vortical structures appear in the lee side ([27]) and interrupt the linearity

of the yawing moment evolution with respect to the yaw angle, as shown later in figure 8. It seems useful to analyze the role of these lee side structures and the corresponding yawing moment non-linearities in the dynamic lateral stability of vehicles.

EXPERIMENTAL SETUP

Wind tunnel characteristics

Measurements are performed in a closed loop wind-tunnel of ISAE (Institut Supérieur de l'Aéronautique et de l'Espace, Toulouse, France). The test section has a square cross-section of 0.45x0.45 m^2 and a length of 0.7 m. The upstream average velocity is U_0=21 m/s corresponding to a Reynolds number of $Re=3.7x10^5$, based on the model length Lref. This Reynolds number is much lower than the one around real ground vehicles but physical mechanisms that will be highlighted around model bluff body in crosswind situations will constitute elements to interpret behavior of full scale vehicle. The turbulence level at the center of the test section is 2%. The free stream velocity and turbulence intensity show a maximum spatial deviation of respectively 1% and 0.5% within the test section. The model is fixed on a turntable that is able to rotate around the vertical axis (figure 1). In order to reduce the thickness of the incoming boundary layer, the turntable is fixed on an elevated floor. The measured thickness is $\delta_{99\%}$=6mm and the boundary layer shape factor (ratio of the displacement thickness to momentum thickness) is 1.31, at 0.41Lref downstream the leading edge.

The wind tunnel coordinates system (X,Y,Z) and the model coordinates system (x,y,Z) are reported in figure 1. The origin of both systems is defined by the turntable center for the X (respectively x) and Y (respectively y) axes and the elevated floor for the Z axis. The Z axis is the

rotation axis. The yaw angle is defined positive ($\beta>0$) when the upstream wind comes from the side of positive y (referred as windward). Leeward refers to the side of negative y.

Oscillating yaw device

The mechanism generating the yaw oscillation is constituted of a rod linking the turntable to the head of a step motor. The set-up generates an amplitude of yaw angle $\Delta\beta=20°$. Different angular ranges can be obtained by using the rod fixation point on the turntable. Two distinct angular ranges are studied: $-10° \leq \beta \leq 10°$ and $10° \leq \beta \leq 30°$. The motor rotation speed fixes the frequency f of the oscillations. Beyond the quasi-static movement reference case obtained at: f=0.2 Hz, three frequencies are studied, i.e. f=1 Hz, f=2 Hz and f=4 Hz. The highest oscillation frequency corresponds to a reduced frequency $f* = 0.053$. This normalized frequency is in the range of the smallest frequencies encountered on road [28].

The movement $\beta(t)$ is measured by an angular probe and is plotted in figure 2 for $f^*=1.325\text{x}10^{-2}$ and , demonstrating a close match with a pure sine function.

Model description

Dynamic yaw effects on flow structures and forces are performed on a simplified car model (figure 3). A complete description of the model, referred as “Willy”, is given in [20]. The analytical definition of the body geometry can be downloaded at http://www.cnam.fr/laboaero/willy.htm. This squareback model presents a geometrical similarity to a mini-van type vehicle. Its rounded edges are showed to prevent any lateral flow separation for moderate yaw angle ($\beta<15°$). As a consequence, this model appears to be well adapted to crosswind studies ([20, 22-24, 27]).

The overall length of the model tested in this paper is Lref=0.28m, the considered reference surface is the maximum cross section, Sref=$7.19 \times 10^{-3} m^2$. The model is mounted on the turntable via four cylindrical struts with a diameter of 8×10^{-3}m ensuring a ground clearance of 12×10^{-3}m.

Measurement methods

Force measurement. Unsteady forces are measured with a force balance internally mounted in the model. Among the full 6 component aerodynamic tensor, the side force F_y and the yawing moment M_Z are the most relevant to characterize when analyzing cross-wind sensitivity of road vehicles [1]. In response to that basic requirement, a simple two-component balance has been designed and manufactured to measure F_y and M_Z. A schematic view of the balance configuration is shown in figure 4a. Force measurements are performed by means of two beam load cells of nominal capacity of 2Kg. The front and rear load cell centers are respectively situated at -/+ 0.19Lref. The measured side force results from the addition of the 2 load cells signals. Figure 4b illustrates the front and rear load cell contributions when applying a point side force $F_{calibration}$ along the x axis. Balance accuracy is estimated to be within 2.5% for the side force and the moment data.

This balance and the model have been custom made to be both light and stiff in order to optimize the dynamic response. A balance dynamic calibration system composed of a mechanical shaker and a reference dynamic force transducer rigidly connected with the balance was applied to characterize the balance response frequency (figure 5, [29]). Exited by a broad band white noise in the range 0-256 Hz, the balance system fixed inside the model showed to measure comparable side force as the reference transducer up to 47 Hz. However, during oscillating tests,

a vibration originating from the plate motion was found to limit the exploitable frequency range of the balance system. Consequently, a low pass filter with a cut-off frequency of 17.5 Hz was then applied to all transient data. Twenty measurement periods of 20s with a data rate of 500 samples per second were performed for each configuration; this protocol was found to give a good statistical convergence of the phase average values with a relative deviation smaller than 0.1%.

For each of the four oscillation frequencies (associated respectively to the reduced frequencies $f^* = 0.265 \times 10^{-2}$, 1.325×10^{-2}, 2.65×10^{-2}, 5.3×10^{-2}), inertial loads are measured without any wind ($U_0=0$) and subtracted to the measured loads for $U_0>0$. This protocol used to isolate pure aerodynamic load is justified by the fact that the yaw movement $\beta(t)$ (and then inertial loads) is checked to be completely independent of U_0.

Particle Image Velocimetry (PIV). PIV measurements are conducted to characterize the flow field along the leeward side of the "Willy" model. Horizontal planes (X,Y) are characterized with a standard 2 component configuration (camera normal to the measurement plane), the vertical velocity component W is not measured. Cross-flow planes (Y,Z) are characterized with a stereoscopic configuration giving access to the 3 components of the velocity vector (U,V,W). PIV configurations are illustrated in figure 6. The pulse laser is an Nd-YAG 2x30 mJ laser with a wave length of 532 nm. The Hisense CCD camera resolution is 1280x1024 pixels. The images cross correlations are performed with the Dantec Dynamics "Flow manager" software. The vector maps have a typical size of 150x187 mm^2 with a spatial resolution of 2.25 mm. To keep this spatial resolution, horizontal velocity fields are obtained from two side by side cameras. A peak

validation filter of 1.2 is applied to analyze the quality of velocity vectors. Reflections interference is minimized using a special fluorescent paint (FP R6G) on the model walls.

Instantaneous velocity fields are obtained from cross-correlation of a pair of images acquired sequentially with a delay of 40μs; presented results correspond to an average of 500 velocity fields registered with an acquisition frequency of 4Hz. For the dynamic case, vectors statistics are associated with phase average at a fixed yaw angle. In that case a specific synchronization device triggers separately "forward motion" $\Delta\beta>0$ (from β=-10° to β=10° for example) and "backward motion" $\Delta\beta<0$ (from β=10° to β=-10° for example). In that case, the acquisition frequency of the pair of images is equivalent to the oscillation frequency. For each selected angle β, two PIV fields are then recorded: one corresponding to the forward motion and the other corresponding to the backward motion.

RESULTS

Steady configuration results

Forces measurements. Side force and yaw moment coefficients, C_y and C_N are showed in figures 7 and 8 for static yaw angles ranging from β=-10° to β=30°. These coefficients are normalized with the maximum cross section Sref, the model length Lref and the free stream dynamic pressure q_0. Results are presented in the model coordinates system and C_N is transported at the origin of the coordinates system.

As observed for real road vehicles ([1]), C_y decreases linearly with β up to yaw angle as large as 40° (figure 7). The yaw moment coefficient C_N rises linearly with β up to $\beta \cong 15°$ (figure 8). For larger yaw angles, a reduction in the slope $dC_N/d\beta$ is observed. The positive destabilising slope $dC_N/d\beta$ is attributed to the unbalance between strong upwind side forces (referred as "front" side forces) and weak downwind side forces (referred as "rear" side forces). When increasing β over 15°, a rise in rear side forces reduces the unbalance and can explain the observed slope reduction ([27]). This explanation is confirmed by the longitudinal position of the centre of pressure $X_{CP}/L_{ref} = C_N/C_y$ (figure 9). Globally, X_{CP} is in forward position which indicates that side forces are dominated by front side forces contribution. For $\beta \geq 15°$, X_{CP} clearly moves backwards, indicating a larger rear side force contribution.

Velocity fields measurements. The cross-flow plane on the rear end of the Willy model (X/Lref=0.5) is analysed for increasing yaw angles from β=10° to β=35°. Figure 10 presents mean velocity field on the lee side of this X-plane, colored by the normalised mean vorticity distribution $\Omega x. L_{ref}/U_0$. From β=10-15°, PIV measurements show the development of two counter-rotating longitudinal structures on the leeward side. The upper one presents a positive vorticity that grows with yaw angle and remains attached to the body wall. The lower one exhibits negative vorticity and tends to move away from the body walls with increasing β. This behaviour is attributed to the interaction of the low structure with the wake of the front leeward strut. These vortical structures were identified similarly in previous studies on the Willy model in static yaw configurations ([22, 27])). They are believed to be responsible for the increase of rear side force contribution, the decrease of the unstable yawing moment and in turn the backward displacement of the centre of pressure for β>15° (figures 8-9).

Velocity fields on the horizontal plane Z/Lref=0.45 show a strong local acceleration on the leeward front side with increasing β (figure 11). The forward position of the centre of pressure (figure 9) originates from this local acceleration associated with a suction peak resulting in a strong local (front) side force. The curvilinear velocity distribution along the leeward side, at 8 mm from the surface, is presented in figure 12 for β=0°,10°,20° and 30°. This distance has been found to be the best compromise to remain as close as possible to the model wall while being outside de boundary layer that develops along the side wall of the body. It is observed that the acceleration peak grows in intensity and moves backward when increasing β. The decrease in velocity with β, for $X \geq$, is attributed to the loss of longitudinal velocity in the upper vortical structure.

Dynamic yaw angle

Dynamic forces measurements. The dynamic response of side force and yawing moment coefficients are presented in figures 13-14 for reduced frequencies ranging from 0.265×10^{-2} to 5.3×10^{-2} and compared to the corresponding static values. Figure 13 refers to the yaw angle range $-10° \leq \beta \leq 10°$ whereas figure 14 refers to the yaw angle range $10° \leq \beta \leq 30°$. In the following, "Forward motion" will refer to the motion from β=-10° to β=10° (or from β=10° to β=30°) while "backward motion" will refer to the motion from β=10° to β=-10° (or from β=30° to β=10°). The lowest reduced frequency $f^* = 0.265 \times 10^{-2}$ seems not very sensitive to the unsteadiness of β and can be considered as "quasi-static". Effectively, for this very low oscillating frequency, the side force and yawing moment coefficients measured in the forward and backward motion are very similar to the corresponding static values. For other frequencies,

$C_y(\beta)$ and $C_N(\beta)$ exhibit an aerodynamic hysteresis loop around the static curves. These hysteresis loops highlight a de-phasing of dynamic curves compared to static curves that grows with the oscillation frequency. The phase lag $\Delta\phi$ is calculated for C_y curves with $\Delta\phi_{C_y} = \beta_{dynamic@C_y} - \beta_{static@C_y}$ and C_N curves with. $\Delta\phi_{C_N} = \beta_{dynamic@C_N} - \beta_{static@C_N}$. Positive $\Delta\phi$ is associated to a delay of dynamic coefficients in forward motion and an advance in backward motion. The observed $\Delta\phi$ always corresponds to a delay of the dynamic coefficient compared to the static coefficient (figures 13, 14, 15). $\Delta\phi$ increases with the frequency and reaches 3° for the lower yaw angle range $-10° \leq \beta \leq 10°$ at $f^*=5.3\times10^{-2}$. Although the side force coefficient presents a similar behavior for the larger yaw range ($10° \leq \beta \leq 30°$), the yaw moment coefficient exhibits a stronger phase lag between 20 and 30°: for $f^*=5.3\times10^{-2}$, 2 peak phase lag of 5° are observed around 28° both in forward and backward motion (figure 15).

Unsteady yaw angle effects on velocity fields. Synchronisation of PIV measurements at a given yaw angle β allows the comparison of velocity fields in forward and backward motions. Considering the same horizontal PIV plane Z/Lref=0.45 as in figure 11, the curvilinear velocity distribution is plotted, distinguishing the forward and backward motions, at $f^*=5.3\times10^{-2}$ and β= 20°, along with the reference static case (figure 16).

It appears interesting to point that the longitudinal velocity differences between forward and backward motion are more pronounced in the pressure recovery area ($X/L_{ref} > -0.3$) whereas they are not visible in the acceleration area ($-0.5 < X/L_{ref} < -0.25$) and weak in the velocity peak area ($X/L_{ref} = -0.3$).

The PIV cross-flow planes on the rear end of Willy (X/Lref=0.5) are presented in figure 17, for the dynamic case $f^*=5.3\times10^{-2}$ and the static case, for β=28°. Unsteadiness of β leads to a

change in longitudinal structures identified on the leeward side: structures visualized in the forward motion present intensities and position equivalent to a smaller static yaw angle whereas structures visualized in the backward motion present intensities and position equivalent to a larger static yaw angle. These observations highlight a delay of longitudinal structures compared to the static case.

DISCUSSION AND PERSPECTIVES

The two tested oscillating cases present a delay in side force and yaw moment response for $f^*>0.265x10^{-2}$ compared to the static case. These two cases differ from the yaw angle ranges: the lower range $-10° \leq \beta \leq 10°$ does not exhibit any leeward vortical structures (see the static cross flow planes in figure 10) whereas upper and lower vortical structures are present on the leeward side for the upper range $10° \leq \beta \leq 30°$ from β=15°. The role of these lateral structures in the dynamic response of aerodynamic efforts can then be discussed.

Even in absence of any lateral vortical structure (β<15°), the delay can reach 3° on C_y and C_N and $f^*=5.3x10^{-2}$ (figure 15). Analyzing velocity fields, this delay seems to originate from the pressure recovery area (figure 16). This point is confirmed by the relative side force measured by the front and the rear load cell of the balance. It clearly appears that the side force coefficient is dominated by the front part contribution but that the rear part is more sensitive to the unsteadiness of the yaw angle and presents stronger phase lag than the front part (figure 18). One can note that surface pressure measurements on a realistic model indicate similarly that the delay between quasi steady and unsteady loads originates from the rear part of the vehicle [21].

Static forces measurements have shown that leeward longitudinal vortices effects are not really visible on global value of C_y but on side force distribution along the body. Their presence is then more visible on C_N with the curve inflection from β=15 ° (figure 8). In dynamic yawing situations, the time delay of vortical structures (figure 10) seems to emphasize the phase lag on C_N that can reach 5° for β=28° and $f^*=5.3x10^{-2}$ (figure 15). For the studied squareback model, the contribution of longitudinal vortices in the dynamic response of the yaw moment is visible but rather weak. For fastback models, these leeward longitudinal vortices issued for the yawing may interact with the backlight longitudinal vortices and introduce a more complex modification on the transient response of aerodynamic efforts. Additional studies on a fastback model are to be performed to compare squareback and fastback sensibility to dynamic yawing and analyse their respective behaviour in link with the flow topology.

CONCLUSIONS

This paper focuses on dynamic yawing effect on the lateral stability of a simplified squareback vehicle. The objectives are to improve the understanding of flow physics interpreting unsteady aerodynamic forces in respect with the unsteady development of the fluid flow around the body. The role of coherent leeward vortical structures on the aerodynamic response to a harmonic crosswind is particularly explored. An existing test bench ([20]) has been extended to create model oscillations within two yaw angle ranges $-10° \leq \beta \leq 10°$ and $10° \leq \beta \leq 30°$. The later presents strong vortical structures on the lee side similar to those observed on real ground vehicles in yawing configurations ([1]). Four reduced oscillation frequencies ranging from $f^*=0.265x10^{-2}$ to $f^*=5.3x10^{-2}$ are studied; the larger one corresponding to the smallest frequencies encountered on road [21].

Static measurements have provided interpretation of global side force and yawing moment evolution with β in link with velocity fields obtained by Particle Image Velocimetry. The velocity peak observed on the front leeward side of the model explains the domination of front side forces and the destabilising resulting yawing moment. Leeward vortical structures appearing from β=15° are shown to induce a weak stabilising effect on the yawing moment.

Model oscillation leads to a delay in side force and yawing moment responses compared to the reference static case. This delay increases with the reduced oscillating frequency. For the larger tested frequency, it can reach five degrees on the yawing moment and appears to be favourable to the lateral stability of the vehicle. This situation would correspond to a decrease of 15% of the yawing moment comparing to the static case for a real vehicle driving at 28 m/s entering within 1.5 seconds in a side gust of 16m/s.

Velocity fields do not present a uniform sensibility to unsteadiness: the delay seems to originate from the pressure recovery area. Moreover, lateral vortical structures increase the delay for the studied squareback model. It is believed that the role of lateral vortical structures will be more pronounced on fastback models, hypothesis to be confirmed with further studies.

ACKNOWLEDGMENTS

The authors would like to thank the technical staff in the Aerodynamic, Energetic and Propulsion Department for their work in construction of the oscillating facility and associated measurement devices.

REFERENCES

[1] Hucho W.H., 1998, *Aerodynamics of road vehicles*, 4rded. SAE International, Chap. 5.

[2] Baker, C. J., 1986. "A Simplified Analysis of Various Types of Wind Induced Road Vehicle Accidents". Journal of Wind Engineering and Industrial Aerodynamics, **22**, pp. 69-85.

[3] Cooper, R., 1984. "Atmospheric turbulence with respect to moving ground vehicles". Journal of Wind Engineering and Industrial Aerodynamics, **17**, pp. 215 - 238.

[4] Baker, C.J., 1991. "Ground Vehicles in High Cross Winds part II: Unsteady Aerodynamic Forces."Journal of Fluids and Structures, **5**, pp. 91 - 111a.

[5] Bearman, P., Mullarkey, S., 1994. "Aerodynamic Forces on Road Vehicles due to Steady Side Winds and Gusts".RAeS Conference on Vehicle Aerodynamics, Loughborough, UK.

[6] Bocciolone, M., Cheli, F., Corradi, R., Muggiasca, S., Tomasini, G., 2008. « Crosswind Action on Rail Vehicles: Wind Tunnel Experimental Analyses". Journal of Wind Engineering and Industrial Aerodynamics, **96**, pp 584 - 610.

[7] Passmore, M.A., Richardson, S., and Imam, A., 2001,."An Experimental Study of Unsteady Vehicle Aerodynamics".*Proc. Institution of Mechanical Engineers*,**215**part D, pp. 779–788.

[8] Baker, C.J. and Humphreys N.D., 1996, "Assessment of the Adequacy of Various Wind Tunnel Techniques to Obtain Aerodynamic Data for Ground Vehicles in Cross Winds". Journal of Wind Engineering and Industrial Aerodynamics,**60**, pp. 49–68.

[9] Sims-Williams, D., 2011, "Cross Winds and Transients: Reality, Simulation and Effects",SAE Technical paperNo.2011-01-0172.

[10] Volpe, R., Da Silva, A., Ferrand, V., Le Moyne, L., 2013. « Experimental and Numerical Validation of a Wind Gust Facility".ASME : J. Fluid Eng., **135**, pp 011106-1-011106-9.

[11] Beauvais, F., 1967. "Transient Nature of Wind Gust Effects on an Automobile.SAE Technical Paper No. 670608.

[12] Cairns, R. S., 1994, "Lateral Aerodynamic Characteristics of Motor Vehicles in Transient Crosswinds". Ph.D. thesis, Cranfield Institute of Technology **.**

[13] Chadwick, A., 1999. C"rosswindAerodynamics of Sports Utility Vehicles, PhD Thesis, Cranfield University, UK.

[14] Tsubokura, M., Nakashima, T., Kitayama, M., Ikawa, Y., Doh, D. H., Kobayashi, T., 2010. “Large Eddy Simulation on the Unsteady Aerodynamic Response of a Road Vehicle in Transient Crosswinds”. International Journal of Heat and Fluid Flow, 31,pp. 1075 - 1086.

[15] Krajnovic, S., Ringqvist, P., Nakade, K., Basara, B., 2012. Large Eddy Simulation of the Flow Around a Simplified Train Moving Through a Crosswind Flow.” Journal of Wind Engineering and Industrial Aerodynamics, 110,pp. 86 - 99.

[16] Dominy, R., Ryan, A., 1999. “An Improved Wind Tunnel Configuration for the Investigation of Aerodynamic Crosswind Gust Response”.SAE Technical Paper No. 1999-01-0808.

[17] Favre, T., Efraimsson, G., 2011. “An Assessment of Detached-Eddy Simulations of Unsteady Crosswind Aerodynamics of Road Vehicles. Flow, Turbulence and Combustion”, **87**, pp.133-163.

[18] Garry, K.P., Cooper, K.R., 1998, “Comparison of Quasi-Static and Dynamic Wind Tunnel Measurements on Simplified Tractor-Trailer Models”, Journal of Wind Engineering and Industrial Aerodynamics,**22**, pp. 185–194.

[19] Mansor, S., and Passmore, M.A., 2007. “Estimation of Bluff Body Transient Aerodynamics Using an Oscillating Model Rig”.Journal of Wind Engineering and Industrial Aerodynamics,**96**, pp. 1218–1231.

[20] Chometon, F., Strzelecki, A., Ferrand, V., Dechipre, H., Dufour, PC.,Gohlke, M., and Herbert, V., 2005, “Experimental Study of Unsteady Wakes Behind an Oscillating Car model”.SAE Technical paperNo. 2005-01-0604.

[21] Wojciak, J., Theissen, P., Heuler, K., Indinger, T., Adams, N., and Demuth, R., 2011, “Experimental Investigation of Unsteady Vehicle Aerodynamics under Time-Dependent Flow Conditions-Part 2”,SAE Technical paper No.2011-01-0164.

[22] Guilmineau, E., and Chometon, F., 2007, “Experimental and Numerical Analysis of the Effect of Side Wind on a Simplified Car Model*”,*SAE Technical paperNo. 2007-01-0108.

[23] Guilmineau, E., and Chometon, F., 2009, “Effect of Side Wind on a Simplified Car Model: Experimental and numerical analysis”,ASME : J. Fluid Eng.,**131**.

[24] Krajnovic, S., Bengtsson, A., and Basara, B., 2011. “Large Eddy Simulation Investigation of the Hysteresis Effects in the Flow around an OscillatingGround Vehicle”,ASME : J. Fluid Eng.*,* **133** .

[25] Diana, G., Resta, F., and Rocchi, D., 2008, "A New Numerical Approach to Reproduce Bridge Aerodynamic non linearities in time domain". Journal of Wind Engineering and Industrial Aerodynamics, **96**, pp. 1871–1884.

[26] Diana, G., Rocchi, D., Argentini, T., and Muggiasca, S., 2010, "Aerodynamic Instability of a Bridge Deck Section Model: Linear and Nonlinear Approach to Force Modeling. Journal of Wind Engineering and Industrial Aerodynamics, **96**, pp. 1871–1884. **98**, pp. 363–374.

[27] Gohlke, M., Beaudoin, J.F., Amielh, M., and Anselmet, F., 2007. "Experimental Analysis of Flow Structures and Forces on a 3D-Bluff-Body in Constant Cross-Wind".Exp Fluids,**43**, pp. 579–594.

[28] Goetz H., 1995. "Crosswind Facilities and Procedures".SAE paper,**1109**.

[29] Kum, R., 1998, "Investigation of the Comparison Method for the Dynamic Calibration of Force Transducers", *Measurements*, **3**, pp. 239–245

LIST OF FIGURES

figure 14. C_y and C_N measured for the reduced frequencies f*= $0.265x10^{-2}$, $1.325x10^{-2}$, $2.65x10^{-2}$, $5.3x10^{-2}$ and $10° \leq \beta \leq 30°$ compared to the corresponding static curve.

figure 15. De-phasing Δ (in degrees) of the dynamic case (f*=$5.3x10^{-2}$) compared to the static case for C_y and C_N. The two yaw ranges $-10° \leq \beta \leq 10°$and $10° \leq \beta \leq 30°$ are presented.

figure 16. $(U^2 + V^2)^{1/2}/U_0$ distribution along the curve C. Comparison of static and dynamic cases.

figure 17. Comparison of static and dynamic (f*=$5.3x10^{-2}$) mean velocity fields at X/lref=0.5 for β=28°, colored by the normalized mean vorticity $\Omega x. L_{ref}/U_0$. Data extracted from PIV measurements.

figure 18. Side force coefficients associated with the front and rear load cell measurements. Static and dynamic cases (f*=$5.3x10^{-2}$) for the two yaw angle ranges $-10° \leq \beta \leq 10°$ and $10° \leq \beta \leq 30°$

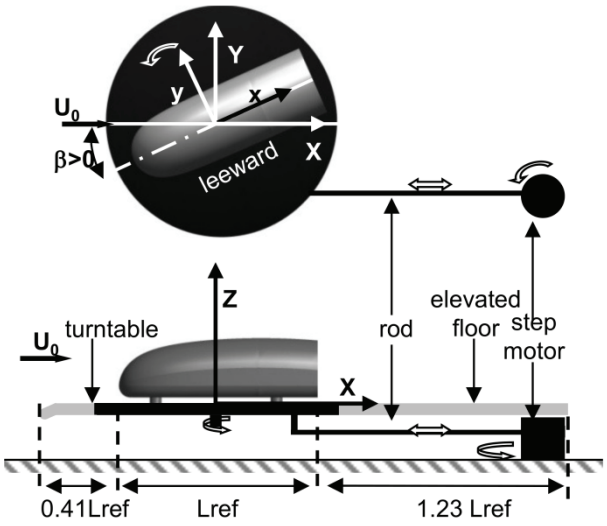

Figure 1 (fig1.tiff)

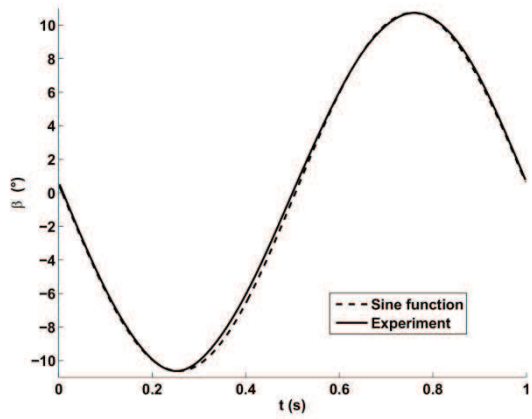

Figure 2 (fig2.tiff)

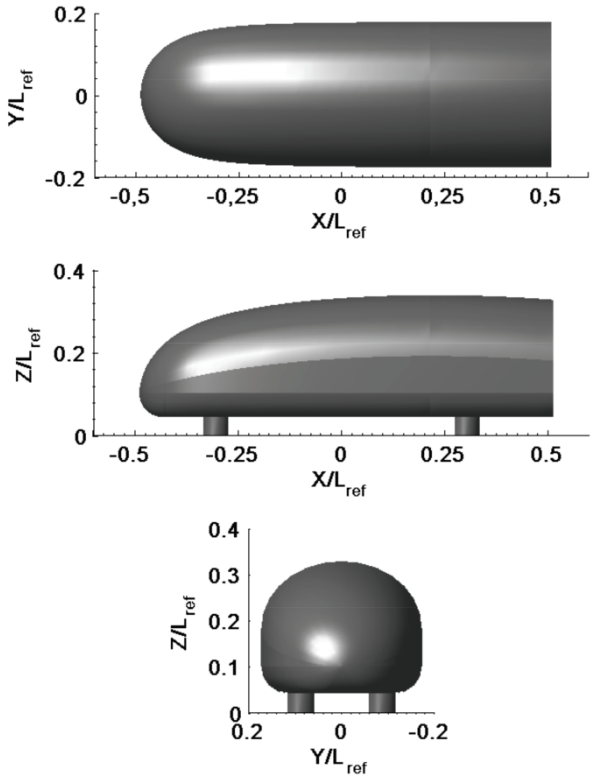

Figure 3 (fig3.tiff)

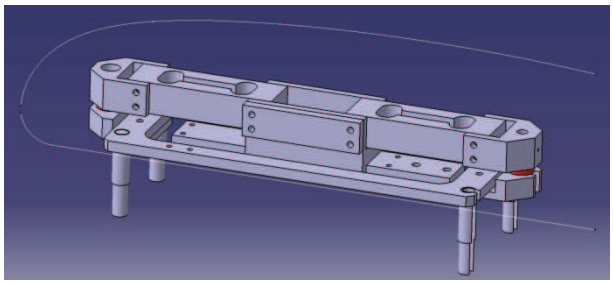

Figure 4a (fig4a.tiff)

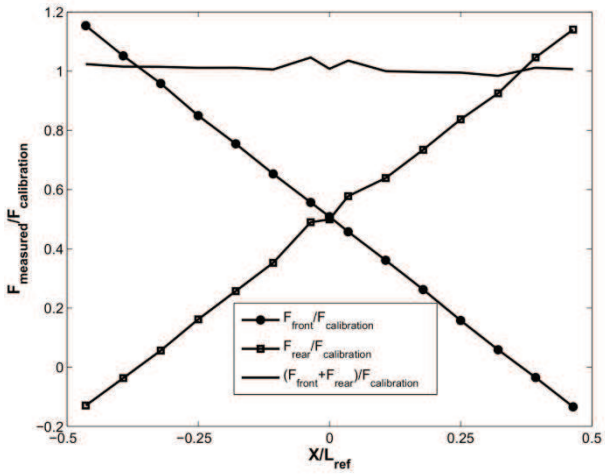

Figure 4b (fig4b.tiff)

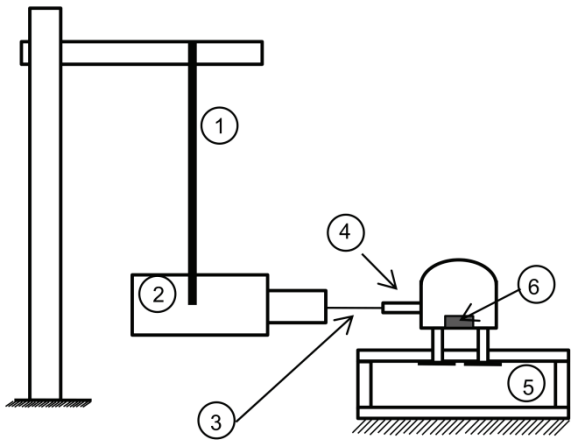

1. elastic rope
2. mechanical shaker
3. rigid sting
4. reference high frequency force transducer
5. heavy steel ingot
6. internal balance

Figure 5 (fig5.tiff)

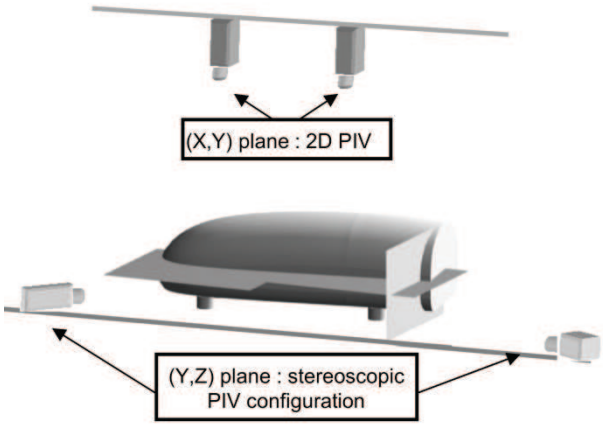

Figure 6 (fig6.tiff)

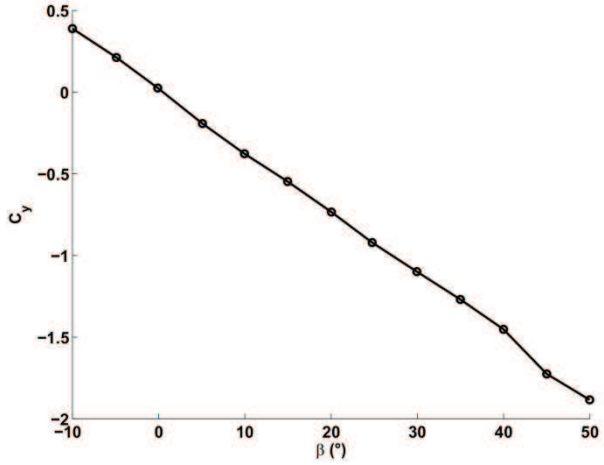

Figure 7 (fig7.tiff)

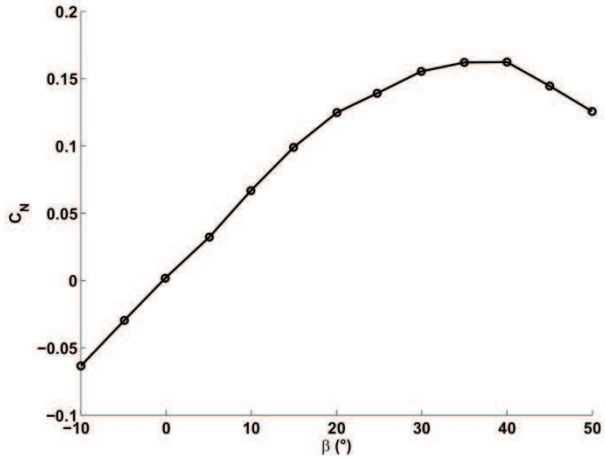

Figure 8 (fig8.tiff)

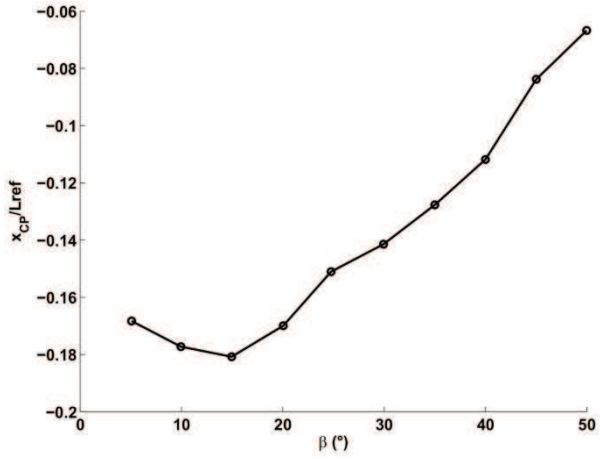

Figure 9 (fig9.tiff)

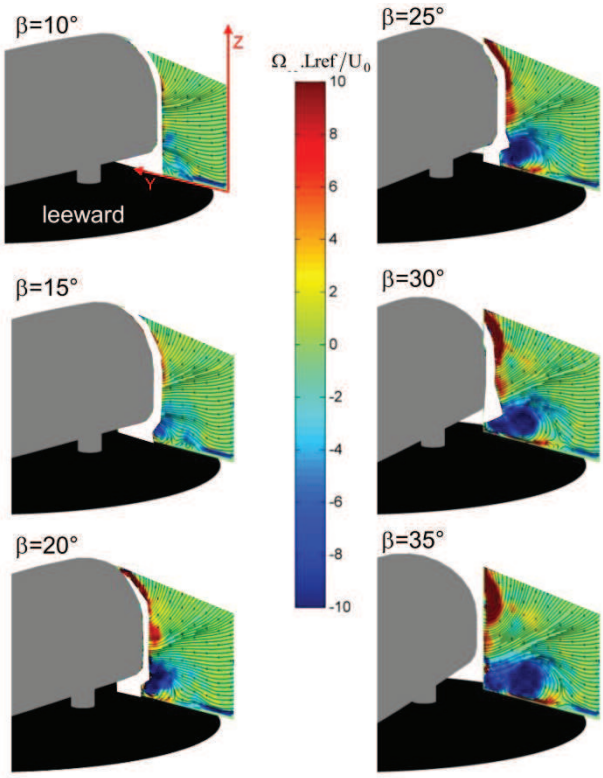

Figure 10 (fig10.tiff)

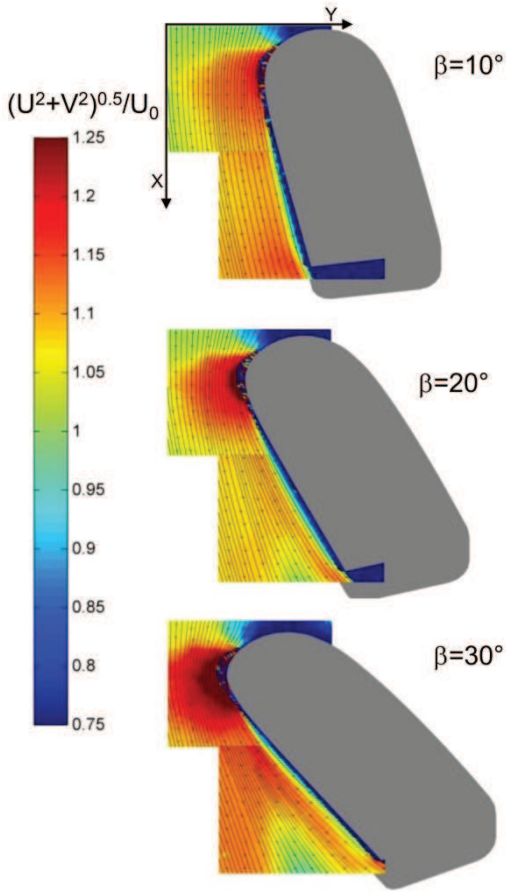

Figure 11 (fig11.tiff)

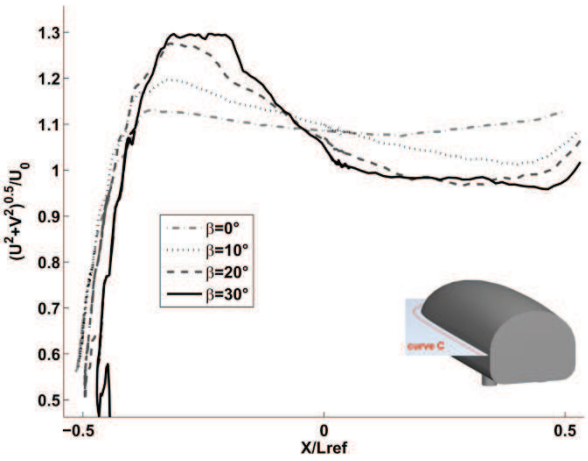

Figure 12 (fig12.tiff)

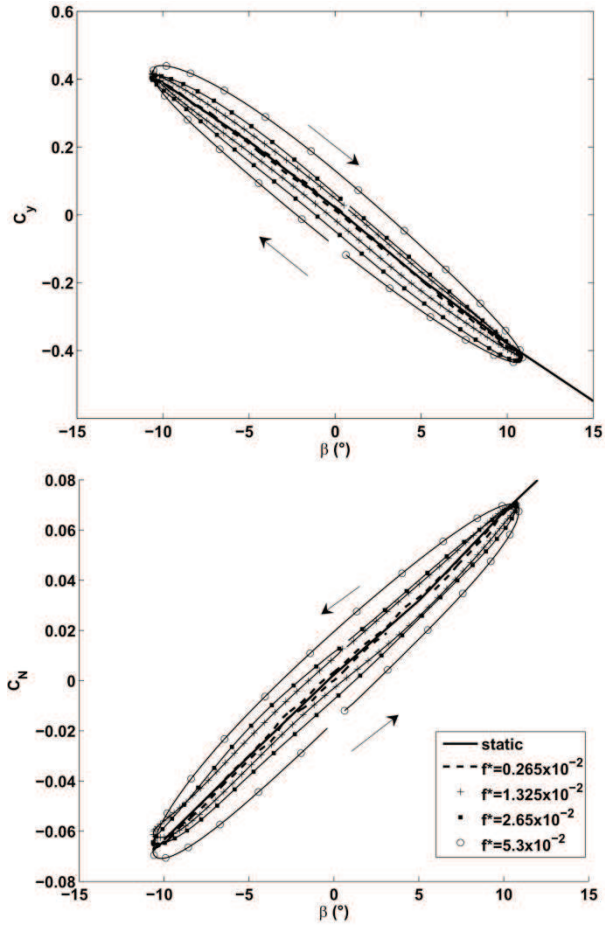

Figure 13 (fig13.tiff)

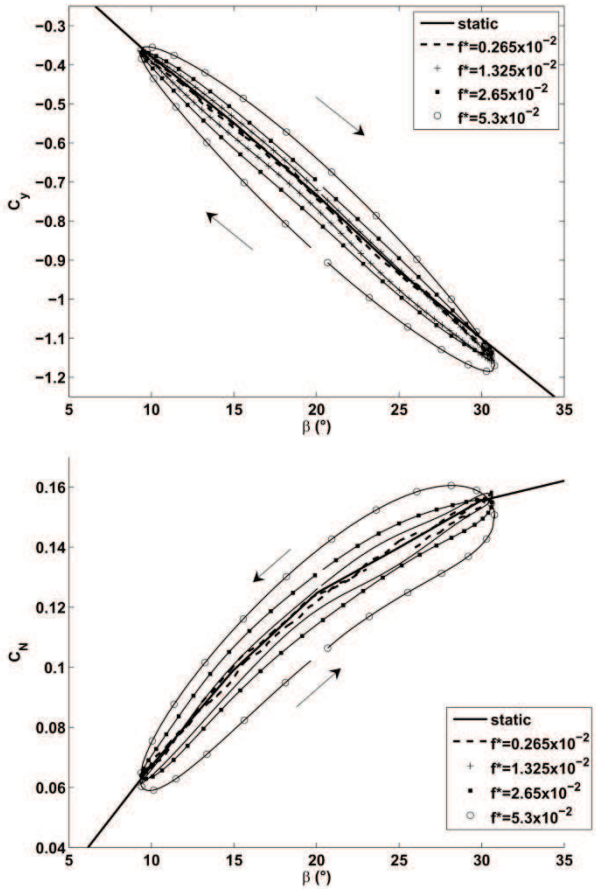

Figure 14 (fig14.tiff)

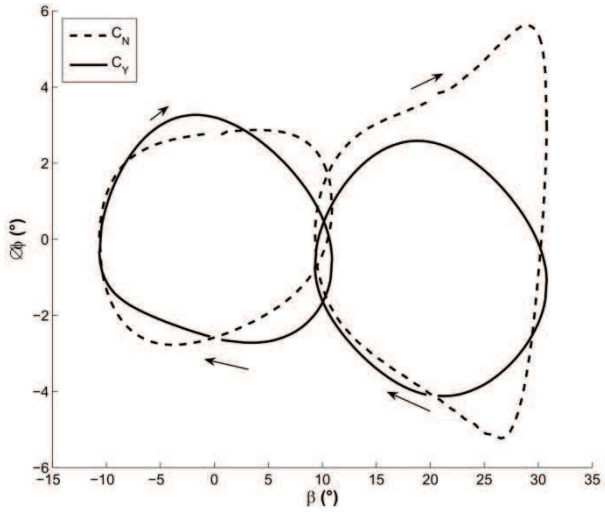

Figure 15 (fig15.tiff)

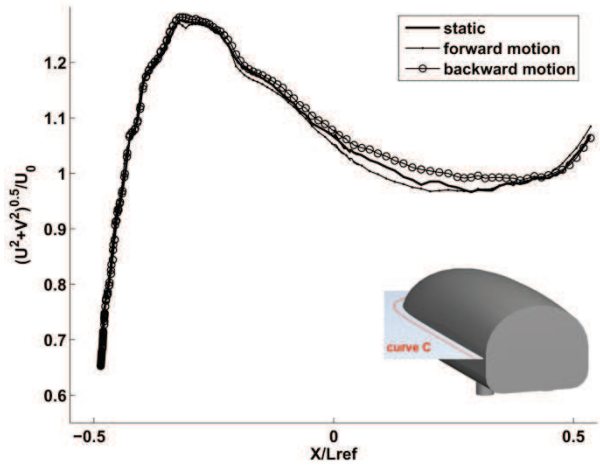

Figure 16 (fig16.tiff)

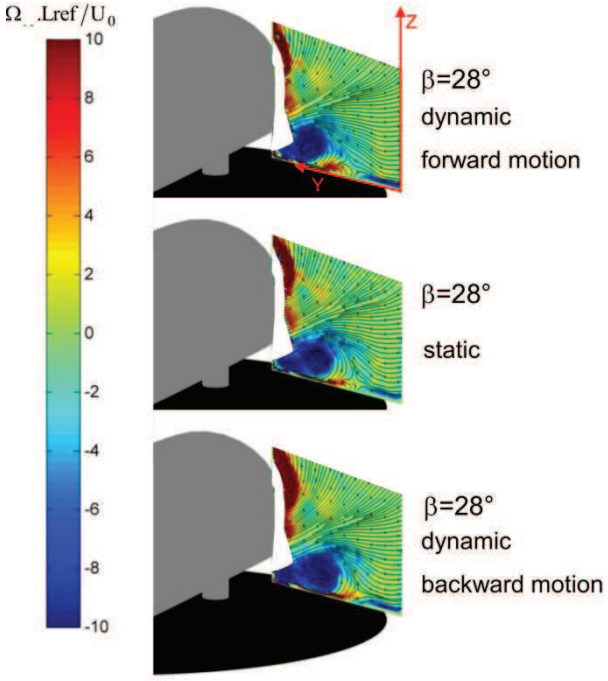

Figure 17 (fig17.tiff)

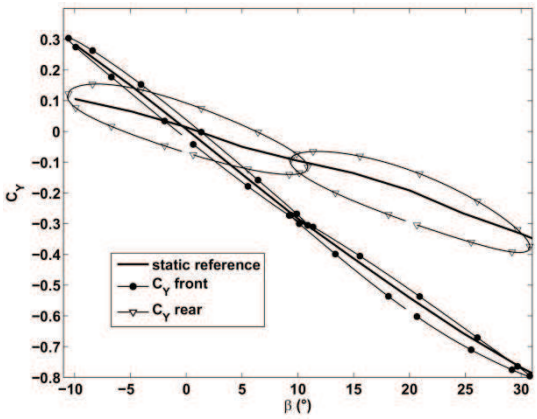

Figure 18 (fig18.tiff)